

Strong coupling of quantized spin waves in ferromagnetic bilayers

Zhizhi Zhang, Huanhuan Yang, Zhenyu Wang, Yunshan Cao, and Peng Yan*

*School of Electronic Science and Engineering and State Key Laboratory of Electronic Thin Films and Integrated Devices,
University of Electronic Science and Technology of China, Chengdu 610054, China*

We formulate a strong-coupling theory for perpendicular standing spin waves (PSSWs) in ferromagnetic bilayers with the interlayer exchange coupling (IEC). Employing the Hoffmann boundary condition and the energy-flow continuity across the interface, we show that the PSSWs are still quantized but with non-integral quantum numbers, in sharp contrast to that of a single layer. The magnon-magnon coupling is characterized by the spectrum splitting which is linear with the IEC in the weak-coupling region, but getting saturated in the strong-coupling limit. Analytical predictions are verified by full micromagnetic simulations with good agreement.

I. INTRODUCTION

Hybrid system combines the advantages of different sub-systems for the exploration of new phenomena and technologies [1, 2]. As a prominent quasi-particle in magnetic system, spin wave and its quantum, magnon, has attracted significant recent attention [3–6] because it can conveniently couple to superconducting resonators and qubits [7–10] that are indispensable for quantum information science and quantum computing [11]. In these studies, the coupling strength, a key parameter to characterize the interconversion between the microwave photons and magnons, has been demonstrated to be proportional to the square root of the number of spins [12, 13]. In practical hybrid structures, different magnetic materials possess their unique features. For example, the metallic ferromagnet like permalloy (Py, $\text{Ni}_{81}\text{Fe}_{19}$) has comparably higher spin density than the ferrite like yttrium iron garnet (YIG, $\text{Y}_3\text{Fe}_5\text{O}_{12}$) [14, 15], while YIG possesses the known lowest damping factor [16].

This prerequisite has intrigued recent interests in magnon-magnon coupling between different magnonic systems, where one of them serves like a “magnonic cavity” [17–21]. Compared with the magnon-photon coupling, the magnon-magnon coupling is exchange interaction dominated and localized at the interface, thus enables the excitation of the quantized perpendicular standing spin waves (PSSWs) and short-wavelength spin waves with high group velocities [22, 23]. The intrinsic PSSW in a single layer manifests a set of discrete modes with wave vectors $n\pi/d$, where d is the film thickness and n is an arbitrary integer [24, 25]. The emerging magnon-magnon coupling allows the magnon transfer and conversion between two magnonic systems with quite distinctive properties. Current interpretations of the magnon-magnon coupling physics relied on the macrospin approximation and the integral-quantized PSSW assumption [17, 18, 20]. When the thickness of magnetic film is shorter than the PSSW wavelength, macrospin model is indeed reasonable by averaging the interlayer exchange coupling (IEC) strength over the entire layer [26, 27]. The integral-quantized PSSW approximation is valid in the limit of weak IEC, where the deviation of the wave vectors from $n\pi/d$ is negligibly small. It has been demonstrated that the frequency splitting between the hybrid modes

is linear with the IEC based on the macrospin model [28–31]. Moreover, it has been shown that a phase shift was induced when spin waves propagate through a hetero-structured interface due to the mismatch of the spin-wave dispersion [32–34]. An open question is how the rather local IEC modifies the PSSW spectrum and the magnon-magnon coupling.

In this work, we theoretically study the magnetization dynamics in exchange-coupled ferromagnetic bilayers. Based on the Hoffmann boundary condition and the energy flow continuity through the interface, we show that the PSSWs are quantized in an unconventional manner with non-integral quantum numbers, in contrast to that of a single layer. The magnon-magnon coupling is linear with the IEC in the weak-coupling region, but saturated in the strong-coupling limit. Micromagnetic simulations compare well with analytical findings.

This paper is organized as follows. In Sec. II, we present the analytical theory to describe the unconventional quantization of PSSWs in ferromagnetic bilayers. Numerical simulations are performed in Sec. III to compare with analytical results. Discussions and conclusions are drawn in Sec. IV.

II. THEORETICAL CONSIDERATIONS

We consider a heterostructure consisting of two magnetic layers, FM_1 and FM_2 with thickness d_1 and d_2 , respectively [see Fig. 1(a)]. The two ferromagnetic films are magnetized along y -direction and are coupled via the exchange interaction at the interface. The magnetization dynamics is governed by the Landau-Lifshitz-Gilbert (LLG) equation:

$$\frac{\partial \mathbf{m}_i}{\partial t} = -\gamma\mu_0 \mathbf{m}_i \times \mathbf{H}_{\text{eff},i} + \alpha_i \mathbf{m}_i \times \frac{\partial \mathbf{m}_i}{\partial t}, \quad (1)$$

where γ is the gyromagnetic ratio, μ_0 is the vacuum permeability, the subscript $i = 1, 2$ labels each layer, $\alpha_i \ll 1$ is the dimensionless Gilbert damping constant, and $\mathbf{m}_i = \mathbf{M}_i/M_{s,i}$ is the unit magnetization vector with $M_{s,i}$ the saturated magnetization. The effective magnetic field $\mathbf{H}_{\text{eff},i}$ comprises the intralayer exchange field $\frac{2A_{\text{ex},i}}{\mu_0 M_{s,i}} \nabla^2 \mathbf{m}_i$ with the exchange constant $A_{\text{ex},i}$, the demagnetization field $\mathbf{H}_d = -m_{i,z} \hat{z}$, the external field $\mathbf{H}_0 = H_0 \hat{y}$, and the interlayer exchange field $\mathbf{H}_{\text{ex},i}$ that is

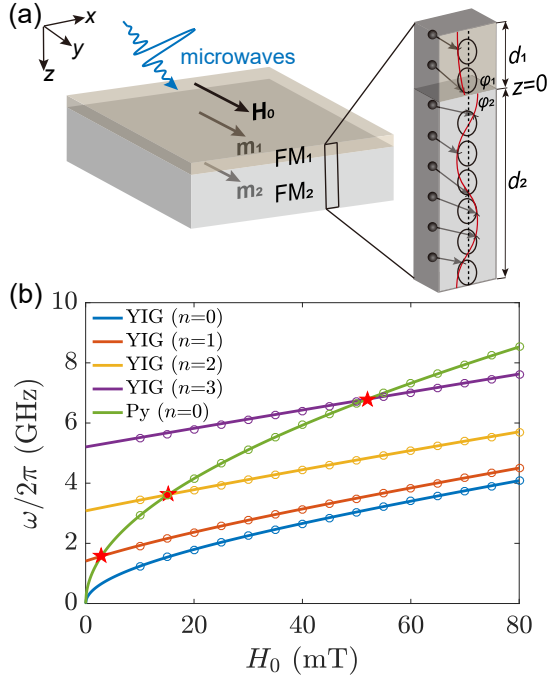


FIG. 1: (a) Schematic of the in-plane magnetized bilayer with thicknesses of d_1 and d_2 , respectively. The inset depicts the PSSW profiles across the two films. (b) Frequencies of the lowest four resonant modes of YIG ($n = 0, 1, 2, 3$) and the Py uniform mode ($n = 0$) as a function of H_0 when $J_{\text{int}} = 0$. Solid curves are the calculations based on Eq. (3). Circles correspond to the micromagnetic simulation results. The red pentagrams indicate the conditions where the two individual layers resonate.

given by:

$$\mathbf{H}_{\text{ex},i} = J_{\text{int}} \mathbf{m}_j \delta(z), \quad (2)$$

where $j \neq i$, $\delta(z)$ is the Dirac function, and $J_{\text{int}} = 2J/\mu_0(M_{s,1} + M_{s,2})$ with the exchange energy density J . Neglecting the damping term and the interlayer exchange term, the spin-wave dispersion relations can be obtained by solving the linearized LLG equation [35]:

$$\omega_i = \gamma \sqrt{\left[\frac{2A_{\text{ex},i}}{M_{s,i}} k_i^2 + \mu_0 H_0 \right] \left[\frac{2A_{\text{ex},i}}{M_{s,i}} k_i^2 + \mu_0 (H_0 + M_{s,i}) \right]}, \quad (3)$$

where k_i is the wave vector of the PSSW. By introducing a complex quantity $m_i^+ = m_{x,i} + im_{z,i}$, the spatial distribution of the PSSW can be expressed as:

$$m_1^+(z) = m_{0,1}^+ \cos(k_1 z + \varphi_1), \quad (4a)$$

$$m_2^+(z) = m_{0,2}^+ \cos(k_2 z + \varphi_2), \quad (4b)$$

where $m_{0,i}^+$ represents the precession amplitude of the PSSW, and φ_i is the magnon phase at the interface. We assume that FM₁ has a higher saturation magnetization and a thinner thickness than FM₂. It is noted that the evanescent wave emerges in the FM₁ layer when the frequency of the PSSW in FM₂ is

lower than the uniform mode in FM₁ [see Fig. 1(b)]. In such a case, Eq. (4a) should be modified to:

$$m_1^+(z) = m_{e,1}^+ \left[\exp\left(\frac{z}{\lambda}\right) + R \exp\left(-\frac{z}{\lambda}\right) \right], \quad (5)$$

with coefficients $m_{e,1}^+$ and R to be determined by the boundary conditions and λ being the decay length. To determine k_i in Eqs. (4), proper boundary conditions should be implemented by integrating Eq. (1) over the vicinity of the top and bottom surfaces ($z = -d_1, d_2$) and the interface ($z = 0$). We assume no pinning at the two surfaces:

$$\left. \frac{\partial m_1^+(z)}{\partial z} \right|_{z=-d_1} = 0, \quad (6a)$$

$$\left. \frac{\partial m_2^+(z)}{\partial z} \right|_{z=d_2} = 0. \quad (6b)$$

Substituting Eqs. (4) into Eqs. (6), we obtain:

$$-k_1 d_1 + \varphi_1 = n_1 \pi, \quad (7a)$$

$$k_2 d_2 + \varphi_2 = n_2 \pi, \quad (7b)$$

where n_1 and n_2 are two arbitrary integers. Instead, substituting Eq. (5) into Eq. (6a), we obtain $R = \exp(-2d_1/\lambda)$, such that:

$$m_1^+(z) = 2m_{e,1}^+ \exp\left(-\frac{d_1}{\lambda}\right) \cosh\left(\frac{z + d_1}{\lambda}\right). \quad (8)$$

At the interface ($z = 0$), the combination of Hoffmann boundary conditions [36, 37] and the magnetic energy-flow conservation across the interface [38] leads to:

$$\frac{2A_{\text{ex},1}}{M_{s,1}} \frac{\partial m_1^+(z)}{\partial z} + J_{\text{int}} [m_2^+(z) - m_1^+(z)] \Big|_{z=0} = 0, \quad (9a)$$

$$-\frac{2A_{\text{ex},2}}{M_{s,2}} \frac{\partial m_2^+(z)}{\partial z} + J_{\text{int}} [m_1^+(z) - m_2^+(z)] \Big|_{z=0} = 0. \quad (9b)$$

Substituting Eqs. (4) into Eqs. (9), we obtain:

$$\left(\frac{-2A_{\text{ex},1}}{M_{s,1}} k_1 \sin \varphi_1 - J_{\text{int}} \cos \varphi_1 \right) m_{0,1}^+ + J_{\text{int}} \cos \varphi_2 m_{0,2}^+ = 0, \quad (10a)$$

$$J_{\text{int}} \cos \varphi_1 m_{0,1}^+ + \left(\frac{2A_{\text{ex},2}}{M_{s,2}} k_2 \sin \varphi_2 - J_{\text{int}} \cos \varphi_2 \right) m_{0,2}^+ = 0. \quad (10b)$$

The resonant condition requires that the determinant of the coefficient matrix of Eqs. (10) vanishes:

$$k_1 k_2 \tan(k_1 d_1) \tan(k_2 d_2) = J_{\text{int}} \left[\frac{M_{s,1}}{2A_{\text{ex},1}} k_2 \tan(k_2 d_2) + \frac{M_{s,2}}{2A_{\text{ex},2}} k_1 \tan(k_1 d_1) \right]. \quad (11)$$

By matching the frequency $\omega_1 = \omega_2$, we are able to solve the wave vectors (k_1 and k_2) and the phases (φ_1 and φ_2) in a self-consistent manner.

In this work, we focus on the coupling between the uniform mode ($k_1 = 0$) in FM₁ and the PSSW mode ($k_2 = n\pi/d_2$) in FM₂ at a certain H_0 . In the absence of the IEC, these two modes are degenerate. Magnon-magnon coupling induces a frequency splitting of the two coupled modes, which can be found by solving Eqs. (3) and (11). It is straight-forward to see that one solution is still $k_1 = 0$ and $k_2 = n\pi/d_2$. Since there

is no explicit expression for other solutions of the transcendental equation (11), we adopt a graphic method. Calculation details are described in Appendix.

Despite of the mentioned difficulty, we can obtain the perturbative solution in the limit of the weak IEC. We consider $J_{\text{int}} \rightarrow 0$, so that $k_1 = \Delta k_1$ and $k_2 = n\pi/d_2 + \Delta k_2$ with $\Delta k_1 \rightarrow 0$ and $\Delta k_2 \rightarrow 0$, and Eq. (11) can be expressed as:

$$(\Delta k_1)^2 d_1 \left(\frac{n\pi}{d_2} + \Delta k_2 \right) (\Delta k_2 d_2) = \frac{J_{\text{int}} M_{s,1}}{2A_{\text{ex},1}} \left(\frac{n\pi}{d_2} + \Delta k_2 \right) (\Delta k_2 d_2) + \frac{J_{\text{int}} M_{s,2}}{2A_{\text{ex},2}} (\Delta k_1)^2 d_1, \quad (12)$$

from which, we obtain:

$$k_1^2 \cong \frac{J_{\text{int}} M_{s,1}}{2A_{\text{ex},1} d_1}, \quad (13)$$

in the weak IEC limit. By differentiating the dispersion relation (3), we obtain the mode splitting:

$$\Delta\omega = \frac{\gamma^2 \mu_0 (M_{s,1} + 2H_0)}{\omega} \frac{J_{\text{int}}}{d_1}. \quad (14)$$

The linear dependence of magnon-magnon coupling on J_{int} is in accordance with the result of the macrospin model [18]. For general J (or J_{int}), the solutions must be found numerically.

III. NUMERICAL RESULTS AND ANALYSIS

To verify our theoretical analysis, full micromagnetic simulations are performed using MUMAX3 to numerically solve the LLG equation (1) [39]. The magnetic parameters of Py and YIG are used for FM₁ and FM₂, respectively. They are: $M_{s,1} = 8.6 \times 10^5$ A/m, $M_{s,2} = 1.48 \times 10^5$ A/m, $A_{\text{ex},1} = 1.3 \times 10^{-11}$ J/m, $A_{\text{ex},2} = 3.1 \times 10^{-12}$ J/m, $\alpha_1 = 0.01$, and $\alpha_2 = 5 \times 10^{-4}$. The thicknesses are $d_1 = 20$ nm and $d_2 = 180$ nm. The $1000 \times 1000 \times 200$ nm³ Py/YIG bilayer structure is discretized by $50 \times 50 \times 80$ cells and periodic boundary conditions (PBC $\times 20$) in x and y directions are applied to simulate the two-dimensional infinite films. The IEC between the two layers is tuned by setting the scaling factor S following Eq. (9) in Ref. [39]. To obtain the spin-wave spectra, a microwave driving field is applied using a “sinc” function $\mathbf{h}(t) = h_0 \sin[\omega_H(t - t_0)]/[\omega_H(t - t_0)]\hat{x}$ with the cut-off frequency $\omega_H/2\pi = 50$ GHz, $t_0 = 0.5$ ns, and $h_0 = 1$ mT. The total simulation time is 100 ns. The spin wave spectra can be analyzed from the fast Fourier transform (FFT) analysis of m_z .

The PSSW spectra of an independent layer can be obtained using a “sinc” excitation localized at the top surface of the layer. The resonant peaks in simulations reproduce the theoretical predictions given by Eq. (3), as shown in Fig. 1(b). It is noted that the Py uniform mode matches with the YIG

PSSW modes $n = 2$ and 3 at $H_0 = 15$ mT and 52 mT (red pentagrams), respectively. It means that the resonant energy can be transferred from one film to another with considerable efficiency if they are coupled. The uniform mode and the first-order PSSW mode frequencies of the single 20-nm thick Py layer are 6.8 and 34.3 GHz respectively at $H_0 = 52$ mT. This frequency gap covers several YIG layer’s intrinsic PSSW modes. Below, we fix the $H_0 = 52$ mT to investigate the IEC effect on PSSW modes. We are interested in the magnon-magnon coupling near the crossing frequency $\omega_c/2\pi = 6.8$ GHz. Since the IEC depends on the nature of the magnetic materials and the growth techniques, the type and strength of the coupling in the metal-oxide bilayers are not clear, particularly considering the complex crystalline and magnetic structure of YIG [40]. Besides, the Ruderman-Kittel-Kasuya-Yosida mechanism induces the oscillation of J between the positive and negative values [41–43]. Therefore, we thoroughly consider the coupled bilayer structure with J ranging from -0.20 to 1.20 mJ/m². The negative value $J = -0.20$ mJ/m² corresponds to the antiferromagnetic exchange field $H_{\text{ex},1} = -42$ mT at the interface.

Figure 2(a) shows the spin wave spectra evolution in bilayer structures with representative J values. The number n indicates that the corresponding mode is derived primarily from the YIG PSSW mode with wave vector $n\pi/d_2$. The notation “YIG” (“Py”) indicates the modes with the intensive dynamic magnetization located in YIG (Py) layer. Specifically, the YIG ($n = 3$) mode and the Py dominant mode can be distinguished by their linewidths near ω_c in the cases of weak coupling. All the spectra as a function of the J values are summarized and color mapped in Fig. 2(b). Figure 2(c) shows the spatial distribution of the PSSW modes with $J = 0.2$ mJ/m². The PSSW modes in the IEC bilayer have the following features: (i) the frequency of the YIG PSSW mode ($n = 3$) remains the same with the intrinsic value ω_c , while the frequency of the Py dominant mode is lower (higher) than ω_c for a negative (positive) J . (ii) The frequency of the Py dominant mode increases monotonically with the weak IEC and saturates at high IEC (J is larger than 0.4 mJ/m²). (iii) The frequencies of higher-order PSSW modes ($n = 4, 5, \dots$) increase smoothly with

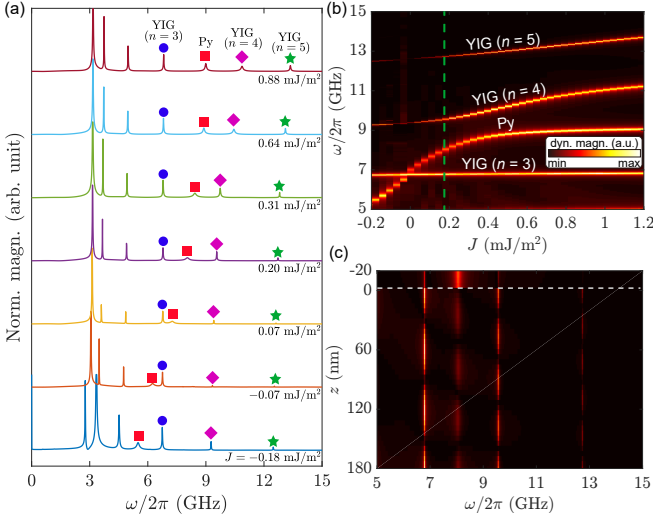


FIG. 2: (a) The PSSW spectra in the bilayer structure with different J . The square, circle, diamond, and pentagram symbols represent the Py dominant mode and the YIG PSSW modes ($n = 3, 4$, and 5), respectively. (b) The PSSW spectra as a function of J . (c) Spatial profiles of PSSW in the bilayer with $J = 0.20$ mJ/m² [labelled by the dashed green line in (b)]. The dashed white line indicates the interface.

the IEC.

Next, we focus on the Py dominant mode, which is highly sensitive to J . The intensive dynamic magnetization in Py layer excites PSSWs in YIG through the exchange torque at the interface [17, 18, 20, 21], which can also be regarded as the coherent spin wave source [44]. The spatial distribution of normalized $|m_z|$ of Py dominant mode in the IEC bilayer with typical IEC values of $J = -0.18$ mJ/m² at 5.5 GHz and $J = 0.20$ mJ/m² at 8.0 GHz are plotted in Fig. 3(a). The spin-wave profiles in the Py layer are sinusoidal for $J > 0$ and exponentially decaying for $J < 0$ (indicating evanescent spin waves as discussed in Sec. II). However, spin-wave profiles in YIG layer appear to be sinusoidal in all cases. In addition, we find that the interface is not the position of the antinode, implying the introduction of a phase shift. To gain a deeper insight, we fit the spin wave profiles using appropriate functions (4) and (5). To obtain the wavevectors, the spin wave profile in YIG is fitted by:

$$|m_z(z)| = m_0 |\cos(k_f z + \varphi_f)|, \quad (15)$$

where m_0 is a scaling factor, k_f and φ_f are the fitting wave vector and phase, respectively. The sinusoidal profiles in Py shorter than half of the wavelength are accurately fitted using the second-order Taylor expansion. Assuming the maximal value located at the top surface ($z = -d_1$), in accordance with the natural boundary condition [Eq. (6)], the following formula is used for fitting the spin-wave profile in Py:

$$|m_z(z)| = m_0 \left(1 - \frac{[(z + d_1)k_f]^2}{2} \right). \quad (16)$$

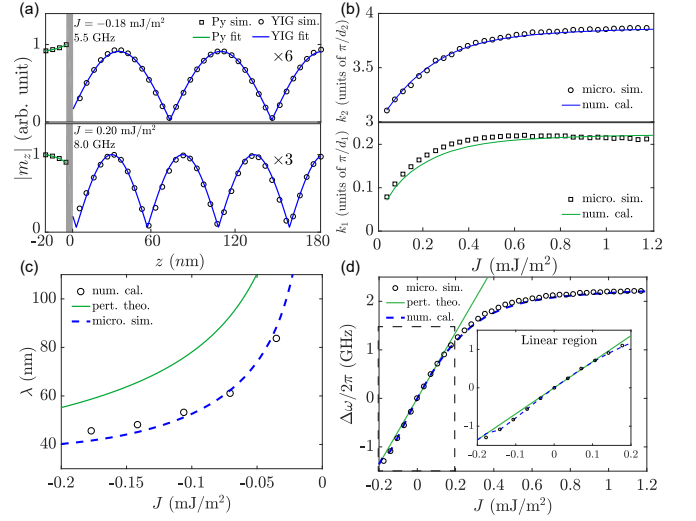


FIG. 3: (a) Spatial distribution of $|m_z|$ of the Py dominant mode in the bilayer with the IEC strength $J = -0.18$ mJ/m² at 5.5 GHz (upper panel) and $J = 0.20$ mJ/m² at 8.0 GHz (lower panel). The patched grey region represents the interface. Squares and circles represent the data in Py and YIG layers, respectively, obtained from micromagnetic simulations. Solid blue and green curves represent the fitting results. Since the spin-wave amplitudes in YIG are too small, we magnify them by 6 or 3 times, as labelled in each part of the figure. (b) Wave vectors in YIG (upper panel) and Py (lower panel) layers as a function of the ferromagnetic IEC strength ($J > 0$). Solid curves represent the numerical solutions of Eqs. (3) and (11) by graphic method (see Appendix). (c) Decay length of the dynamic magnetization in the Py layer as a function of the antiferromagnetic IEC strength ($J < 0$). The green line represents the analytical formula (13). (d) Frequency splitting as a function of J . Inset shows the zoomed in linear regime indicated as in the dashed box. The solid green curves in (c) and (d) represent the formula (14). The dashed blue curves in (c) and (d) represent the numerical solutions by graphic method (see Appendix). All symbols in (b), (c) and (d) represent the results from full micromagnetic simulations.

The exponentially decaying profile in Py below ω_c can be fitted by:

$$|m_z(z)| = a \exp(-z/\lambda_f) + b \exp(z/\lambda_f), \quad (17)$$

where a and b are two scaling parameters, and λ_f is the fitting decay length.

Figure 3(b) shows the wave vectors as a function of positive J . Both k_1 and k_2 increase rapidly near $J = 0$ and saturate for large J . For the antiferromagnetic IEC ($J < 0$), the decaying length λ in the Py layer versus the J is plotted in Fig. 3(c). With the increasing of the antiferromagnetic IEC strength, the spin-wave decay length decreases rapidly. Numerical solutions based on the graphic method compare very well with the full micromagnetic simulations. However, we note that the perturbation theory can only qualitatively predict the λ . The reason is that when $J \rightarrow 0$, a small variation of J leads to large λ change because of the inversely-proportional relation between them, i.e., $\lambda \propto 1/\sqrt{|J|}$, according to Eq. (13). Frequency splitting ($\Delta\omega$) between the coupled modes as

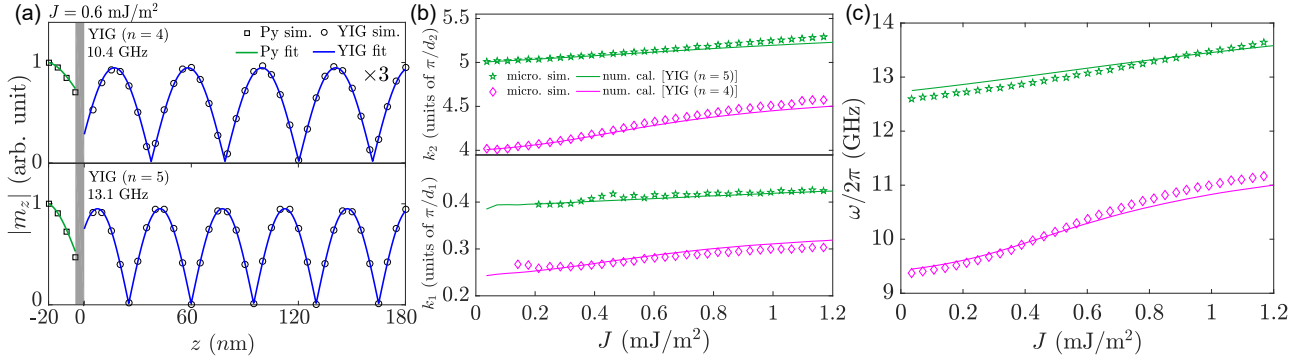


FIG. 4: (a) Spatial distribution of $|m_z|$ for the YIG ($n=4$) mode at 10.4 GHz (upper panel) and the YIG ($n=5$) mode at 13.1 GHz (lower panel) in the bilayer with $J = 0.6 \text{ mJ/m}^2$. Since the spin-wave amplitude in YIG ($n=4$) mode is too small, we magnify them by 3 times, as labeled in the figure. (b) Wave vectors in YIG (upper panel) and Py (lower panel) layers. (c) Frequencies of the YIG ($n=4$ and 5) modes as a function of J . The magenta and green colors represent the YIG ($n=4$ and 5) modes respectively. Diamond and pentagram symbols correspond to the micromagnetic simulation results. Solid curves represent the numerical solutions by graphic method (see Appendix).

a function of the IEC strength is presented in Fig. 3(d). The perturbation theory [Eq. (14)] matches very well with both micromagnetic simulations and numerical calculations for J ranging from -0.2 to 0.2 mJ/m^2 [inset of Fig. 3(d)]. However, the perturbation theory becomes invalid beyond the weak IEC range and $\Delta\omega$ is saturated after $J > 0.4 \text{ mJ/m}^2$. The reason for the saturation will be discussed below.

It is worthy mentioning that the YIG modes ($n=4$ and 5) have significant frequency shifts beyond the weak IEC limit, as shown in Fig. 2(b). The profiles of the dynamic magnetization in both Py and YIG layers are sinusoidal, as shown in Fig. 4(a). Figure 4(b) plots the k_1 and k_2 of these modes as a function of J . Their frequencies can be evaluated by the dispersion relations, as plotted in Fig. 4(c). Micromagnetic simulations (symbols) agree well with the numerical calculations (curves).

Physically, the IEC torque exerted on the spins is proportional to $J\mathbf{m}_1(0) \times \mathbf{m}_2(0)$, favoring the uniform precession with positive J at the interface. In the presence of a strong IEC, $\mathbf{m}_1(0)$ becomes parallel with $\mathbf{m}_2(0)$ [45, 46]. An even stronger IEC strength does not facilitate more interaction between the quantized magnons in the two layers. This scenario explains the saturation of $\Delta\omega$ and the frequency shifts of the higher modes with J . In such case, φ_1 is equal to φ_2 in Eq. (7), leading to $(k_1d_1 + k_2d_2)/\pi = n, n \in \mathbb{N}$. Generally, the quantum number k_id_i/π indicates how many half-wavelengths are contained within the layer. It reveals that the sum $(k_1d_1 + k_2d_2)/\pi$ in the coupled bilayer becomes an integer in the strong IEC region, even though the number k_id_i/π does not.

To verify this picture, we extend the theoretical analysis to $J = 2.1 \text{ mJ/m}^2$ and perform additional micromagnetic simulations. The dependence of $(k_1d_1 + k_2d_2)/\pi$ on J is plotted in Fig. 5. Taking the YIG ($n=4$) mode as an example, the intrinsic mode is excited around 9.4 GHz. At this frequency, k_1d_1/π is equal to 0.24 according to the dispersion relation [Eq. (3)]. It increases to 0.35 with $J \rightarrow \infty$. Accordingly, k_2d_2/π varies from 4 to 4.65 [Fig. 4(b)]. For this mode, $(k_1d_1 + k_2d_2)/\pi$ approaches to the next integral number 5 at $J = 2.1 \text{ mJ/m}^2$,

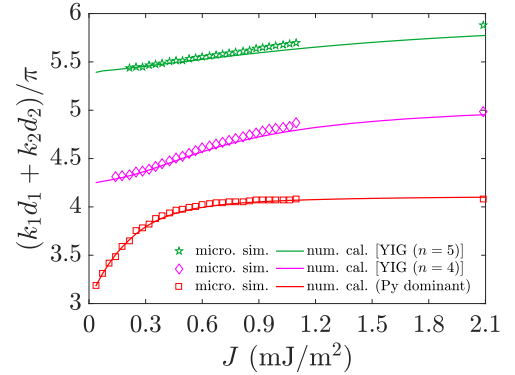


FIG. 5: Sum of the wave number $(k_1d_1 + k_2d_2)/\pi$ in the coupled bilayer as a function of J . Symbols are micromagnetic simulation results. Solid curves represent the data based on numerical solutions by graphic method (see Appendix).

indicated as the magenta curves and symbols in Fig. 5. Meanwhile, $(k_1d_1 + k_2d_2)/\pi$ for YIG ($n=5$) mode keeps increasing in this wide J range. It suggests that the precessions of $\mathbf{m}_1(0)$ and $\mathbf{m}_2(0)$ in this mode remain unparallel.

IV. DISCUSSION AND CONCLUSION

In the above analysis, the parameters of YIG and Py are used for analysis. We point out that the proposed theory is applicable for general IEC bilayers. Experimentally, the known strongest IEC reported on the garnet/metal heterostructure is 0.86 mJ/m^2 , which was grown on the silicon substrate [47]. Even stronger IEC can be achieved with the improvement of the interface quality [48]. Our results open a new perspective for the precise measure of the IEC strength in a wider range. The sensitivity of the frequency splitting can be used to determine the IEC strength [45]. The frequency shifts of the higher-order PSSW modes can serve as the calibration in the

strong IEC region.

In summary, we investigated the IEC effects on the PSSW modes in ferromagnetic bilayers. In sharp contrast to common wisdom, we showed that the magnon-magnon coupling characterized by the frequency splitting is linear with IEC in the weak coupling limit but saturated in the strong coupling region. The frequency shifts of higher-order PSSW modes possess higher sensitivity to the IEC than the fundamental mode in the strong coupling region. Our findings are helpful for analytically understanding the strong magnon-magnon coupling in magnetic heterostructures and for precisely measuring the IEC strength in a wide range.

V. ACKNOWLEDGEMENTS

We thank Z.-X. Li for helpful discussions. This work was supported by the National Natural Science Foundation of China (Grants No. 12074057, No. 11604041, and No. 11704060). Z. Z. acknowledges the financial support of the China Postdoctoral Science Foundation under Grant No. 2020M673180. Z. W. acknowledges the financial support of the China Postdoctoral Science Foundation under Grant No. 2019M653063.

APPENDIX: GRAPHIC METHOD TO SOLVE THE TRANSCENDENTAL EQUATION

Using the parameters in Sec. III, the dispersion relations are plotted as the blue curves in Fig. 6. It is noted that when $k_2 \geq 3\pi/d_2$ ($k_2 < 3\pi/d_2$), the identity $\omega_1(k_1) = \omega_2(k_2)$ can be established with k_1 to be a real (purely imaginary) number, as shown by symbols in Figs. 6(a)-6(d) [Figs. 6(e) and 6(f)].

The boundary condition curves are plotted as the orange curves in Figs. 6(a)-6(f). The intersections between the blue and orange curves are the solutions for the PSSW modes. The blue circle, corresponding to the YIG ($n = 3$) mode, is consistently located at $(k_1, k_2) = (0, 3\pi/d_2)$. In the ferromagnetic IEC cases ($J > 0$) [Figs. 6(a) and 6(b)], the red square symbol, corresponding to the Py dominant mode, moves rapidly at a lower J value, approaching to the asymptotic line $k_2 = 4\pi/d_2$. It is noted that the red square and the blue circle coincide at $(k_1, k_2) = (0, 3\pi/d_2)$ with $J = 0$. The purple rhombus and the green pentagram, corresponding to the YIG ($n = 4$ and 5) modes respectively, are shifted from $k_2 = n\pi/d_2$ toward $k_2 = (n + 1)\pi/d_2$ ($n = 4$ and 5) with the increase of J . The boundary condition curve becomes flat when J exceeds 2.0 mJ/m^2 (see Supplemental movie CurveEvolution1.gif). In this case, the coordinations (k_1, k_2) of the purple rhombus (green pentagram) satisfy that $k_1 d_1 + k_2 d_2 \cong 5\pi$ ($k_1 d_1 + k_2 d_2 \cong 6\pi$). Meanwhile, in the antiferromagnetic IEC ($J < 0$) cases, the purple rhombus (green pentagram) moves little away from the horizontal line $k_2 = 4\pi/d_2$ ($k_2 = 5\pi/d_2$) with k_1 a real number, as shown in Figs. 6(c) and 6(d). The red square is found with k_1 a purely imaginary number, as shown

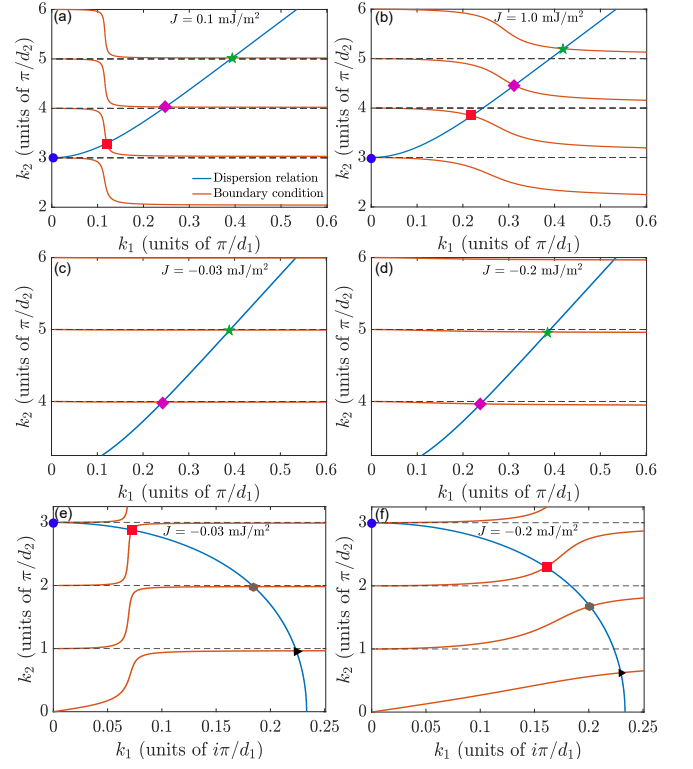


FIG. 6: Dispersion relations (blue curves) [Eq. (3)] with $\omega_1 = \omega_2$ and boundary conditions (orange curves) [Eq. (11)] to graphically determine k_1 and k_2 : with $J = 0.1 \text{ mJ/m}^2$ (a), $J = 1.0 \text{ mJ/m}^2$ (b), $J = -0.03 \text{ mJ/m}^2$ (c), and $J = -0.2 \text{ mJ/m}^2$ (d), where k_1 is a real number; and with $J = -0.03 \text{ mJ/m}^2$ (e) and $J = -0.2 \text{ mJ/m}^2$ (f), where k_1 is purely imaginary number. The square, triangle, hexagon, circle, rhombus, and pentagram symbols represent solutions of the Py dominant mode and the YIG PSSW modes ($n = 1, 2, 3, 4$ and 5), respectively.

in Figs. 6(e) and 6(f). If the antiferromagnetic IEC strength increases, the red square approaches to the horizontal line $k_2 = 2\pi/d_2$ (see Supplemental movie CurveEvolution2.gif).

* Corresponding author: yan@uestc.edu.cn

- [1] G. Kurizki, P. Bertet, Y. Kubo, K. Mølmer, D. Petrosyan, P. Rabl, and J. Schmiedmayer, Quantum technologies with hybrid systems, *Proc. Natl. Acad. Sci. U.S.A.* **112**, 3866 (2015).
- [2] Z.-L. Xiang, S. Ashhab, J. Q. You, and F. Nori, Hybrid quantum circuits: Superconducting circuits interacting with other quantum systems, *Rev. Mod. Phys.* **85**, 623 (2013).
- [3] D. Lachance-Quirion, Y. Tabuchi, A. Gloppe, K. Usami, and Y. Nakamura, Hybrid quantum systems based on magnonics, *Appl. Phys. Express* **12**, 070101 (2019).
- [4] M. Harder and C.-M. Hu, in *Solid State Physics*, Vol. 69, edited by R. E. Camley and R. L. Stamps (Academic Press, 2018) Chap. 2, pp. 47-121.
- [5] B. Bhoi and S.-K. Kim, in *Solid State Physics*, Vol. 70, edited by R. L. Stamps and H. Schultheiss (Academic Press, 2018) Chap. 1, pp. 1-77.
- [6] Y. Li, W. Zhang, V. Tyberkevych, W.-K. Kwok, A. Hoffmann,

- and V. Novosad, Hybrid magnonics: Physics, circuits, and applications for coherent information processing, *J. Appl. Phys.* **128**, 130902 (2020).
- [7] H. Huebl, C. W. Zollitsch, J. Lotze, F. Hocke, M. Greifenstein, A. Marx, R. Gross, and S. T. B. Goennenwein, High Cooperativity in Coupled Microwave Resonator Ferrimagnetic Insulator Hybrids, *Phys. Rev. Lett.* **111**, 127003 (2013).
- [8] L. McKenzie-Sell, J. Xie, C.-M. Lee, J. W. A. Robinson, C. Ciccarelli, and J. A. Haigh, Low-impedance superconducting microwave resonators for strong coupling to small magnetic mode volumes, *Phys. Rev. B* **99**, 140414(R) (2019).
- [9] Y. Tabuchi, S. Ishino, A. Noguchi, T. Ishikawa, R. Yamazaki, K. Usami, and Y. Nakamura, Coherent coupling between a ferromagnetic magnon and a superconducting qubit, *Science* **349**, 405 (2015).
- [10] J.-K. Xie, S.-L. Ma, and F.-L. Li, Quantum-interference-enhanced magnon blockade in an yttrium-iron-garnet sphere coupled to superconducting circuits, *Phys. Rev. A* **101**, 042331 (2020).
- [11] A. V. Chumak, V. I. Vasyuchka, A. A. Serga, and B. Hillebrands, Magnon spintronics, *Nat. Phys.* **11**, 453 (2015).
- [12] Y. Cao, P. Yan, H. Huebl, S. T. B. Goennenwein, and G. E. W. Bauer, Exchange magnon-polaritons in microwave cavities, *Phys. Rev. B* **91**, 094423 (2015).
- [13] J. M. Fink, R. Bianchetti, M. Baur, M. Göppl, L. Steffen, S. Filipp, P. J. Leek, A. Blais, and A. Wallraff, Magnon spintronics, Dressed Collective Qubit States and the Tavis-Cummings Model in Circuit QED, *Phys. Rev. Lett.* **103**, 083601 (2009).
- [14] J. T. Hou and L. Liu, Strong Coupling between Microwave Photons and Nanomagnet Magnons, *Phys. Rev. Lett.* **123**, 107702 (2019).
- [15] Y. Li, T. Polakovic, Y.-L. Wang, J. Xu, S. Lendinez, Z. Zhang, J. Ding, T. Khaire, H. Saglam, R. Divan, J. Pearson, W.-K. Kwok, Z. Xiao, V. Novosad, A. Hoffmann, and W. Zhang, Strong Coupling between Magnons and Microwave Photons in On-Chip Ferromagnet-Superconductor Thin-Film Devices, *Phys. Rev. Lett.* **123**, 107701 (2019).
- [16] Y. Kajiwara, K. Harii, S. Takahashi, J. Ohe, K. Uchida, M. Mizuguchi, H. Umezawa, H. Kawai, K. Ando, K. Takanashi, S. Maekawa, and E. Saitoh, Transmission of electrical signals by spin-wave interconversion in a magnetic insulator, *Nature (London)* **464**, 262 (2010).
- [17] Y. Xiong, Y. Li, M. Hammami, R. Bidthanapally, J. Sklenar, X. Zhang, H. Qu, G. Srinivasan, J. Pearson, A. Hoffmann, V. Novosad, and W. Zhang, Probing magnon-magnon coupling in exchange coupled $\text{Y}_3\text{Fe}_5\text{O}_{12}$ /Permalloy bilayers with magneto-optical effects, *Sci. Rep.* **10**, 12548 (2020).
- [18] Y. Li, W. Cao, V. P. Amin, Z. Zhang, J. Gibbons, J. Sklenar, J. Pearson, P. M. Haney, M. D. Stiles, W. E. Bailey, V. Novosad, A. Hoffmann, and W. Zhang, Coherent Spin Pumping in a Strongly Coupled Magnon-Magnon Hybrid System, *Phys. Rev. Lett.* **124**, 117202 (2020).
- [19] J. Chen, C. Liu, T. Liu, Y. Xiao, K. Xia, G. E. W. Bauer, M. Wu, and H. Yu, Strong Interlayer Magnon-Magnon Coupling in Magnetic Metal-Insulator Hybrid Nanostructures, *Phys. Rev. Lett.* **120**, 217202 (2018).
- [20] S. Klingler, V. Amin, S. Geprägs, K. Ganzhorn, H. Maier-Flaig, M. Althammer, H. Huebl, R. Gross, R. D. McMichael, M. D. Stiles, S. T. B. Goennenwein, and M. Weiler, Spin-Torque Excitation of Perpendicular Standing Spin Waves in Coupled YIG/Co Heterostructures, *Phys. Rev. Lett.* **120**, 127201 (2018).
- [21] H. Qin, S. J. Hämäläinen, and S. van Dijken, Exchange-torque-induced excitation of perpendicular standing spin waves in nanometer-thick YIG films, *Sci. Rep.* **8**, 5755 (2018).
- [22] C. Liu, J. Chen, T. Liu, F. Heimbach, H. Yu, Y. Xiao, J. Hu, M. Liu, H. Chang, T. Stueckler, S. Tu, Y. Zhang, Y. Zhang, P. Gao, Z. Liao, D. Yu, K. Xia, N. Lei, W. Zhao, and M. Wu, Long-distance propagation of short-wavelength spin waves, *Nat. Commun.* **9**, 738 (2018).
- [23] K. An, V. Bhat, M. Mruczkiewicz, C. Dubs, and D. Grundler, Optimization of spin-wave propagation with enhanced group velocities by exchange-coupled ferrimagnet-ferromagnet bilayers, *Phys. Rev. Applied* **11**, 034065 (2019).
- [24] Y. S. Gui, N. Mecking, and C. M. Hu, Quantized Spin Excitations in a Ferromagnetic Microstrip from Microwave Photo-voltage Measurements, *Phys. Rev. Lett.* **98**, 217603 (2007).
- [25] A. Navabi, C. Chen, A. Barra, M. Yazdani, G. Yu, M. Montazeri, M. Aldosary, J. Li, K. Wong, Q. Hu, J. Shi, G. P. Carman, A. E. Sepulveda, P. K. Amiri, and K. L. Wang, Efficient excitation of high-frequency exchange-dominated spin waves in periodic ferromagnetic structures, *Phys. Rev. Applied* **7**, 034027 (2017).
- [26] B. Heinrich, Y. Tserkovnyak, G. Woltersdorf, A. Brataas, R. Urban, and G. E. W. Bauer, Dynamic Exchange Coupling in Magnetic Bilayers, *Phys. Rev. Lett.* **90**, 187601 (2003).
- [27] Y. Tserkovnyak, A. Brataas, G. E. W. Bauer, and B. I. Halperin, Nonlocal magnetization dynamics in ferromagnetic heterostructures, *Rev. Mod. Phys.* **77**, 1375 (2005).
- [28] S. Zhang, J. Rong, H. Wang, D. Wang, and L. Zhang, Spin-wave resonance frequency in ferromagnetic thin film with interlayer exchange coupling and surface anisotropy, *Surf. Sci.* **667**, 79 (2018).
- [29] S. Li, Q. Li, J. Xu, S. Yan, G.-X. Miao, S. Kang, Y. Dai, J. Jiao, and Y. Lü, Tunable optical mode ferromagnetic resonance in FeCoB/Ru/FeCoB synthetic antiferromagnetic trilayers under uniaxial magnetic anisotropy, *Adv. Funct. Mater.* **26**, 3738 (2016).
- [30] W. Wang, P. Li, C. Cao, F. Liu, R. Tang, G. Chai, and C. Jiang, Temperature dependence of interlayer exchange coupling and gilbert damping in synthetic antiferromagnetic trilayers investigated using broadband ferromagnetic resonance, *Appl. Phys. Lett.* **113**, 042401 (2018).
- [31] S. Li, G.-X. Miao, D. Cao, Q. Li, J. Xu, Z. Wen, Y. Dai, S. Yan, and Y. Lü, Stress-enhanced interlayer exchange coupling and optical-mode FMR frequency in self-bias FeCoB/Ru/FeCoB trilayers, *ACS Appl. Mater. Interfaces* **10**, 8853 (2018).
- [32] M. Mailian, O. Gorobets, Y. Gorobets, M. Zelent, and M. Krawczyk, Exchange spin waves transmission through the interface between two antiferromagnetically coupled ferromagnetic media, *J. Magn. Magn. Mater.* **484**, 484 (2018).
- [33] M. Milian, O. Gorobets, Y. Gorobets, M. Zelent, and M. Krawczyk, Control of the spin wave phase in transmission through the ultrathin interface between exchange coupled ferromagnetic materials, *Acta Phys. Pol. A* **133**, 480 (2018).
- [34] R. Verba, V. Tiberkevich, and A. Slavin, Spin-wave transmission through an internal boundary: Beyond the scalar approximation, *Phys. Rev. B* **101**, 144430 (2020).
- [35] B. A. Kalinikos and A. N. Slavin, Theory of dipole-exchange spin wave spectrum for ferromagnetic films with mixed exchange boundary conditions *J. Phys. C: Solid State Phys.* **19**, 7013 (1986).
- [36] F. Hoffmann, A. Stankoff, and H. Pascard, Evidence for an exchange coupling at the interface between two ferromagnetic films, *J. Appl. Phys.* **41**, 1022 (1970).
- [37] F. Hoffmann, Dynamic pinning induced by nickel layers on permalloy films, *Phys. Stat. Sol. b* **41**, 807 (1970).
- [38] A. I. Akhiezer, V. G. Bar'yakhtar, and S. V. Peletminskii, *Spin Waves* (Amsterdam: North-Holland, 1968).
- [39] A. Vansteenkiste, J. Leliaert, M. Dvornik, M. Helsen, F. Garcia-

- Sanchez, and B. Van Waeyenberge, The design and verification of mumax3, *AIP Adv.* **4**, 107133 (2014).
- [40] S. Geller and M. Gilleo, The crystal structure and ferrimagnetism of yttrium-iron garnet, $\text{Y}_3\text{Fe}_2(\text{FeO}_4)_3$, *J. Phys. Chem. Solid.* **3**, 30 (1957).
- [41] M. A. Ruderman and C. Kittel, Indirect exchange coupling of nuclear magnetic moments by conduction electrons, *Phys. Rev.* **96**, 99 (1954).
- [42] T. Kasuya, A Theory of Metallic Ferro- and Antiferromagnetism on Zener's Model, *Prog. Theor. Phys.* **16**, 45 (1956).
- [43] K. Yosida, Magnetic properties of Cu-Mn alloys, *Phys. Rev.* **106**, 893 (1957).
- [44] V. D. Poimanov, A. N. Kuchko, and V. V. Kruglyak, Magnetic interfaces as sources of coherent spin waves, *Phys. Rev. B* **98**, 104418 (2018).
- [45] M. Vohl, J. Barnaś, and P. Grünberg, Effect of interlayer exchange coupling on spin-wave spectra in magnetic double layers: Theory and experiment, *Phys. Rev. B* **39**, 12003 (1989).
- [46] K. Vayhinger and H. Kronmüller, Spin wave theory of exchange coupled ferromagnetic multilayers, *J. Magn. Magn. Mater.* **72**, 307 (1988).
- [47] Y. Fan, P. Quarterman, J. Finley, J. Han, P. Zhang, J. T. Hou, M. D. Stiles, A. J. Grutter, and L. Liu, Manipulation of coupling and magnon transport in magnetic metal-insulator hybrid structures, *Phys. Rev. Applied* **13**, 061002 (2020).
- [48] C. Morrison, J. J. Miles, T. N. Anh Nguyen, Y. Fang, R. K. Dumas, J. Åkerman, and T. Thomson, Exchange coupling in hybrid anisotropy magnetic multilayers quantified by vector magnetometry, *J. Appl. Phys.* **117**, 17B526 (2015).